ADVANCED FUNCTIONAL MATERIALS
www.afm-journal.de

Nanoconfined $LiBH_4$ as a Fast Lithium Ion Conductor

Didier Blanchard, Angeloclaudio Nale, Dadi Sveinbjörnsson, Tamara M. Eggenhuisen, Margriet H. W. Verkuijlen, Suwarno, Tejs Vegge, Arno P. M. Kentgens, and Petra E. de Jongh**

Designing new functional materials is crucial for the development of efficient energy storage and conversion devices such as all solid-state batteries. $LiBH_4$ is a promising solid electrolyte for Li-ion batteries. It displays high lithium mobility, although only above 110 °C at which a transition to a high temperature hexagonal structure occurs. Herein, it is shown that confining $LiBH_4$ in the pores of ordered mesoporous silica scaffolds leads to high Li^+ conductivity (0.1 mS cm^{-1}) at room temperature. This is a surprisingly high value, especially given that the nanocomposites comprise 42 vol% of SiO_2. Solid state ^7Li NMR confirmed that the high conductivity can be attributed to a very high Li^+ mobility in the solid phase at room temperature. Confinement of $LiBH_4$ in the pores leads also to a lower solid-solid phase transition temperature than for bulk $LiBH_4$. However, the high ionic mobility is associated with a fraction of the confined borohydride that shows no phase transition, and most likely located close to the interface with the SiO_2 pore walls. These results point to a new strategy to design low-temperature ion conducting solids for application in all solid-state lithium ion batteries, which could enable safe use of Li-metal anodes.

1. Introduction

The need to transform our society into one based on renewable energy resources poses a grand challenge for science: to design low-cost material systems based on abundant materials that enable the efficient conversion and storage of renewable energy. Rechargeable lithium-ion batteries are standard in today's consumer portable electronics, but substantial improvements are needed to achieve higher energy densities, safer use, longer lifetimes and reduced cost to meet the demand for example in the transport sector and grid-scale storage of renewable electricity.[1,2] Conventional Li-ion batteries use electrolytes made of organic liquids or gels. They have high Li^+ conductivity, but are flammable, causing safety issues, and allow lithium dendrite formation at the electrode-electrolyte interface. These dendrites cause a decrease of the cell capacity, reducing their lifetime, not to mention the possibility of hazardous short circuits.[1,3,4]

All solid-state batteries are an alternative to the current state-of-the-art lithium-ion batteries. Solid electrolytes enable the assembly of all solid-state cells with superior thermal and mechanical stability (no leakage). Furthermore, energy and power densities can be increased. Lithium metal can be used as anode,[5] it has higher gravimetric energy density than any materials used with liquid electrolytes and as dendrite formation is suppressed, the space between the electrodes can be reduced. However, while research on solid electrolytes has been conducted over the past few decades, no viable solution has emerged on the market so far. The challenge is to develop solid electrolytes with sufficient chemical and electrochemical stability, while offering high lithium ionic conductivity and negligible electronic conduction.[6] A Li^+ conductivity of at least 1 mS cm^{-1} is often cited as the minimum conductivity required for electrolytes in consumer batteries[7,8] with electrode separator of thicknesses < 25 µm.[9] For example 1 M $LiPF_6$ in ethyl-methyl carbonates, a widely used organic liquid electrolyte, has a Li^+ conductivity of 12 mS cm^{-1} at 27 °C.[10]

Regarding solid electrolytes, only a few classes of materials with sufficiently high ionic conductivity have been reported, including some Perovskite and Garnet type oxides[11–14] and compounds of the NASICON[15,16] and LISICON families.[17] However, they have some critical drawbacks such as low electrochemical decomposition potential, instability towards contact with elemental lithium and/or too high electronic conductivity.

$LiBH_4$ is an example of the family of complex metal hydrides, solids with an ionic lattice, composed of metal cations (in this case Li^+) and complex hydride anions (in this case BH_4^-). The family includes other borohydrides such as $NaBH_4$

Dr. D. Blanchard, Dr. D. Sveinbjörsson, Prof. T. Vegge
Department of Energy Conversion and Storage
Technical University of Denmark
Frederiksborgvej 399, DK-4000, Roskilde, Denmark
E-mail: dibl@dtu.dk
Dr. A. Nale, Dr. T. M. Eggenhuisen, Dr. Suwarno, Prof. P. E. de Jongh
Inorganic Chemistry and Catalysis
Debye Institute for Nanomaterials Science
Utrecht University
Universiteitsweg 99, 3584 CG, Utrecht, The Netherlands
E-mail: P.E.deJongh@uu.nl
Dr. M. H. W. Verkuijlen, Prof. A. P. M. Kentgens
Institute for Molecules and Materials
Radboud University
Heyendaalseweg 135, 6525 AJ, Nijmegen, The Netherlands

DOI: 10.1002/adfm.201402538

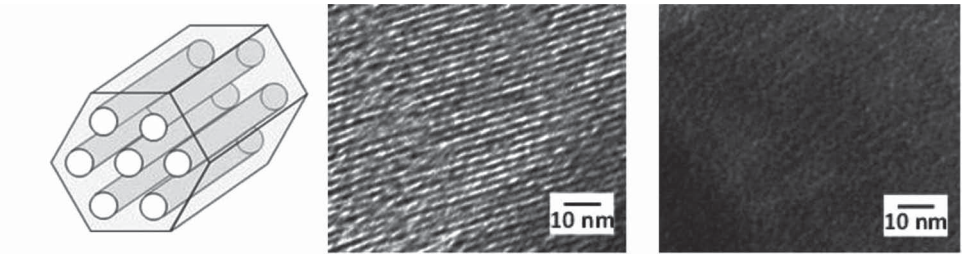

Figure 1. Left: schematic representation of the porosity in the MCM-41 ordered mesoporous silica scaffolds used to confine the $LiBH_4$, showing a cut out comprising only 7 pores; Middle: bright field transmission electron micrograph of a detail of a SiO_2 scaffold particle with 4.0 nm pore size; Right: dark field electron micrograph of a the same SiO_2 scaffold after melt-infiltration with $LiBH_4$.

and $Mg(BH_4)_2$, and aluminum hydrides such as $LiAlH_4$ and $NaAlH_4$. Complex metal hydrides are in wide use as reductants in organic synthesis, but it is only recently that their remarkable properties and thus their potential as energy storage and conversion materials have been recognized. Lithium borohydride has been investigated extensively, both as a hydrogen storage material[18–22] and as a crystalline solid electrolyte material for lithium batteries.[23–26] It is lightweight (0.666 g/cm^3) and has been shown to be electrochemically stable up to 5 V.[27] $LiBH_4$, like virtually all metal borohydrides, can be found in different polymorphs, depending on pressure and temperature. The orthorhombic *Pnma* phase, which is the stable phase at room temperature, has a low ionic conductivity (~10^{-5} mS cm^{-1} at 30 °C). However, the hexagonal *P63/mmc* phase, firstly described as $P6_3mc$,[28] which is stable at temperatures above 110 °C under atmospheric pressure, has a remarkable high ionic conductivity (~1 mS cm^{-1} at 120 °C). The phase transition can be shifted to lower temperatures by replacing a fraction of the BH_4^- anions by somewhat larger halide anions (I^-, Br^- or Cl^-),[29–31] leading to high Li^+ conductivity even at room temperature. However, in the case of bromine and chlorine substitution, phase segregation occurs with time,[32,33] while the $LiBH_4$-LiI solid solution electrochemical stability window is reduced to 3 V.[34]

It is well established that interfacial effects and reduction of the dimensions of solid materials by confinement in nanopores can induce profound changes in functionality, although studies have mostly been limited to the impact on the melting temperatures for solids such as ice, polymer and metals.[35–39] Investigations on $LiBH_4$ confined in nanoporous carbon scaffolds have been reported by several groups.[40–45] Interestingly, high hydrogen mobilities were reported at room temperature, based on nuclear magnetic resonance (NMR) and quasi-elastic neutron scattering (QENS) measurements, and attributed to reorientational jumps of the BH_4^- units. However, carbon materials have significant electronic conductivity and rather wide pore size distributions with heterogeneous pore morphologies. This hampers not only detailed studies on pore size effects, for instance by NMR,[46,47] but also conductivity measurements and precludes the use of such materials as solid electrolytes.

In contrast, silica has a very low electronic and ionic mobility, which makes it an attractive scaffold to investigate confinement effects on ionic conductivity and mobility. Ordered mesoporous silica scaffolds with highly uniform and tunable pore sizes and morphologies are available,[48] making them particularly suitable to systematically study confinement effects. The fact that most studies have focused on carbon scaffolds is undoubtedly related to the high reactivity of $LiBH_4$ and its decomposition products with oxides. However, we recently reported a successful strategy to completely fill the pores of silica scaffolds with $LiBH_4$ by melting infiltration, applying high hydrogen pressures during heating to prevent reaction.[49,50]

Here, we present for the first time a study on the impact of nanoconfining $LiBH_4$ in ordered mesoporous SiO_2 scaffolds on its structural phase transition, Li^+ ionic mobility and ionic conductivity. We show that confinement of $LiBH_4$ in the nanopores of silica scaffolds changes the stability of the different structural phases and yields, even at room temperature, high ionic conductivities owing to fast lithium mobility. This is of great relevance to the use of the nanocomposite as a solid electrolyte for all solid-state batteries.

2. Results and Discussion

2.1. Confining Lithium Borohydride in Nanoporous Silica

For this study we employed ordered mesoporous silica scaffolds. These scaffolds are unique in the sense that they present highly ordered porosity, with monodisperse pore sizes tunable from ≈1.5 to 30 nm. We specifically used MCM-41 type scaffolds, with pores that run parallel while being 2D hexagonally ordered (*P6mm* symmetry) as schematically depicted in **Figure 1** (left frame). N_2 physisorption yields a total pore volume of 0.88–0.97 cm^3 g^{-1} for the scaffolds that we used. Their well-defined cylindrical pore geometry allows very accurate pore size determination from the analysis of the N_2 desorption branch using Non-linear Density Functional Theory calculations. It yielded pore diameters of 4.0–4.5 nm. Figure 1 (middle frame), shows a bright field electron micrograph of an empty SiO_2 mesoporous scaffold, illustrating the ordered nature and monodispersity of the porosity.

After melt-infiltration of this scaffold with $LiBH_4$ (sample LS-91), the pore structure of the silica is hardly discernable anymore (Figure 1, right frame). The starkly reduced contrast is due to the limited density difference between SiO_2 and $LiBH_4$, and a first evidence of the fact that the pores of the silica scaffold are filled with $LiBH_4$. Further evidence comes from EELS detection, which confirms the presence of B in the silica matrix. On a macroscopic scale, the successful melt infiltration of the porous SiO_2 matrix with $LiBH_4$ is evidenced by the loss of pore volume upon addition of the $LiBH_4$. Also the sharp decrease in the fingerprint of crystalline $LiBH_4$ in X-ray diffraction after

sample preparation, which confirms the presence of nanoconfined $LiBH_4$ that lacks long-range crystallinity.[41] Complementary results on the pore diameters and the evidences of the pore filling are provided in the Supporting Information.

2.2. Impact of Pore-Confinement on the Structural Phase Transition

For bulk $LiBH_4$, the high Li^+ ionic mobility is directly tied to the solid-solid structural phase transition around 115 °C, thus we first investigated the impact of nanoconfinement on the temperature of the phase transition using differential scanning calorimetry (DSC). Calorimetry is a very suitable technique to detect phase transitions, even if the phases are not crystalline, via heat evolution or absorption. With $LiBH_4$, the measurements are far from trivial as normally upon heating it starts to decompose around the melting point.[51] Hence it requires calorimetric equipment that combines high temperatures with hydrogen pressure to prevent decomposition of the $LiBH_4$ prior to or upon melting. **Figure 2** (upper frame) shows a representative DSC measurement for bulk crystalline $LiBH_4$ cycling the temperature between 50 and 300 °C. Upon heating, the low-temperature orthorhombic phase, first an endothermic signal (corresponding to the solid-solid phase transition at 115 °C to form the high-mobility hexagonal $LiBH_4$ phase) is detected, followed by a second endothermic signal (corresponding to melting) at 285 °C. Upon cooling, solidification of the $LiBH_4$ is observed with the same onset temperature. Upon further cooling, the solid $LiBH_4$ reverts to the low-temperature phase. The DSC measurements show that under applied hydrogen pressure all phase transitions are fully reversible. Furthermore,

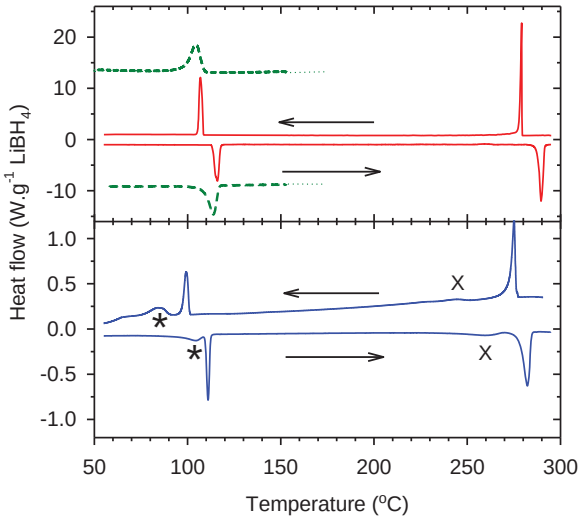

Figure 2. Scanning differential calorimetric measurements showing the heat effects occurring for bulk $LiBH_4$ (upper frame) and melt infiltrated $LiBH_4$ in mesoporous silica of 4.0 nm pores (MI-91 – lower frame) upon temperature cycling between 50 and 300 °C with 5 °C/min under 20 bar H_2 atmosphere. The green dash line (upper frame) is for the physical mixture of $LiBH_4$ and mesoporous silica prior to melt infiltration (PM-91). Note the different scales in the upper and lower frames. The green traces have been translated along the Y-axis. (*) phase transition and (×) melting of the confined $LiBH_4$.

the solid-solid phase transition for a physical mixture of SiO_2 and $LiBH_4$ is presented as a dotted curve (sample PM-91). The phase transition peak is slightly broadened, which can be ascribed to the poor heat conductivity of the added SiO_2, but a single peak with an onset at the same temperature as for pure $LiBH_4$ is observed, and the enthalpy measured is in accordance with the amount of $LiBH_4$ in the sample. This shows that heating and cooling in this temperature range does not cause any reaction between the SiO_2 and the $LiBH_4$.

In the lower frame of Figure 2, an example of the heat effects for the same sample after melt infiltration, that is, with $LiBH_4$ confined in the pores of a silica scaffold with 4.0 nm pore size, is shown (sample MI-91). Similar sharply defined thermal events as for bulk $LiBH_4$ are observed at 110 and 281 °C. This is because a larger amount of $LiBH_4$ has been used than the corresponding pore volume of the silica matrix and a fraction of $LiBH_4$ is present in crystalline grains outside the SiO_2 pores. Signals from nanoconfined $LiBH_4$ are also observed and the features, with an onset around 250 °C, are due to the melting and solidification of the borohydride located into the pores. The melting point depression is about 30 °C compared to crystalline $LiBH_4$. Indeed, it has been well-established that nanoconfinement can shift melting points to considerable lower temperatures, due to the significant contribution of the interfacial energy.[38] Considering the temperature range between 50 and 120 °C, next to the crystalline $LiBH_4$ transition around 115 °C, additional features are observed at significantly lower temperatures, with an onset around 90 °C. Given the temperature range, it is safe to ascribe these features to a solid-solid structural phase transition for the nanoconfined phase. Thus, a clear effect of nanoconfinement is to significantly reduce the temperatures for the phase transitions, both for the solid-to-liquid as well as the solid-to-solid phase transition. Here again, the measurements show that under applied hydrogen pressure, all phase transitions are fully reversible.

For bulk $LiBH_4$, enthalpies of 2.23 and 4.66 kJ mol^{-1} for the solid-to-solid and solid-to-liquid phase transitions were measured. They are 50–60% of the tabulated enthalpies of 4.18 kJ mol^{-1} and 7.6 kJ mol^{-1} for the structural phase transition and for the melting and solidification, respectively.[52] This is most likely related to the unusual high hydrogen pressure during the measurements (20 bar), causing heat leakage due to the high thermal conductivity of the hydrogen gas, although a minor contribution to the loss of active phase by oxidation or reaction with air containing trace amounts of water during handling and transport of the $LiBH_4$ cannot be strictly excluded. We used the ratio between experimental and theoretical enthalpy values for the pure $LiBH_4$ samples as a calibration of the enthalpy for the nanocomposite samples that were measured under exactly the same experimental conditions. The values of enthalpies found for the solid-solid phase transition of the nanoconfined $LiBH_4$ are much lower (about a factor five) than the enthalpy for the crystalline $LiBH_4$ structural phase transition. It could be that the specific phase transition enthalpy is reduced and/or that not all nanoconfined $LiBH_4$ undergoes a solid-solid phase transition (see the following sections).

The phase transitions enthalpies at 281 °C and 110 °C allow direct quantification of the amount of $LiBH_4$ that is not confined in the pores, and hence of the amount of nanoconfined

$LiBH_4$. Reproducibility within one measurement (quantifying the solid-solid transition enthalpy comparing heating and cooling run) was generally within 2%. The standard deviation for multiple measurements on identical samples, as well as comparing the $LiBH_4$ solid-solid phase transition enthalpies for a series of physical mixtures was 6–9%. This quantification was compared with the values estimated from the decrease in X-ray crystallinity upon melt-infiltration, assuming that none of the nanopore confined $LiBH_4$ contributes significantly, because of the lack of long range ordering, to the peak intensities. This yields with an error of 5–8% the crystalline fraction in the samples.[46] As a matter of fact, both estimates, from calorimetry and XRD agree remarkably well for all samples. We should mention that the pore filling obviously depends on the mass ratio of $LiBH_4$ to SiO_2. However, for the same $LiBH_4$ loading (42–44 wt% $LiBH_4$) samples with different degrees of pore filling were obtained, 60% (sample MI-60) and 91% (sample MI-91), while with a loading of 35 wt% $LiBH_4$, 81% was obtained (sample MI-81). The variation is most probably related to the mixing and resulting heterogeneity of the SiO_2 scaffold and $LiBH_4$ blend prior to the melt infiltration. This variation allows us to compare samples with nominally the same composition, but considerably different fraction of the $LiBH_4$ in the pores.

2.3. Lithium Ionic Mobility and Conductivity

2.3.1. Electrochemical Impedance Spectroscopy

Electrochemical Impedance spectroscopy (EIS) measurements performed on the nanocomposite yield Nyquist plots consisting of single, slightly depressed semi-circles (See **Figure 3**, top right frame for representative examples). Although this suggests that only one process contributes to the ionic conduction, we cannot exclude that concurrent processes like bulk, grain boundary or interfacial conduction exist, but overlap in the Nyquist plots, as in this case it is not possible to separate these different contributions using only impedance spectroscopy.[53,54] The Nyquist plots are fitted using an (*RQ*) equivalent circuit model, i.e., a resistor and a constant phase element in parallel (schematic on Figure 3). The intersection of the semicircle with the *Z'* axis in the low-frequency limit gives the pellet resistance, *R*. The conductivity of the electrolyte is then given by:

$$\sigma = \frac{d}{AR} \tag{1}$$

where *d* is the thickness of the pressed nanocomposite and *A* the surface area of the pellet. Arrhenius plots for the conductivity of SiO_2-$LiBH_4$ nanocomposites, with 60 (sample MI-60) and 91% (sample MI-91) pore filling, together with the one for bulk $LiBH_4$ and the physical mixture obtained prior to the melt-infiltration of MI-91 (noted PM-91), are shown in Figure 3, left frame. The slight hysteresis during temperature cycling can be ascribed to a small temperature lag, as the thermocouple is not directly in contact with the pellet, rather than to intrinsic sample properties.

For bulk $LiBH_4$, a remarkable jump in the conductivity, three orders of magnitude, occurs at the phase transition temperature. Indeed at temperatures below 110 °C, $LiBH_4$ adopts the poorly Li^+ conducting orthorhombic structure, while above this temperature it adopts the hexagonal highly conducting structure.[23,55] For the nanocomposites, the first striking observation is that no large jump in conductivity is observed around the bulk $LiBH_4$ solid-solid phase transition temperature. For MI-60, only a slight increase is observed, while for MI-91 an almost monotonic evolution in the conductivity with rising temperature is observed for the whole temperature range. The second

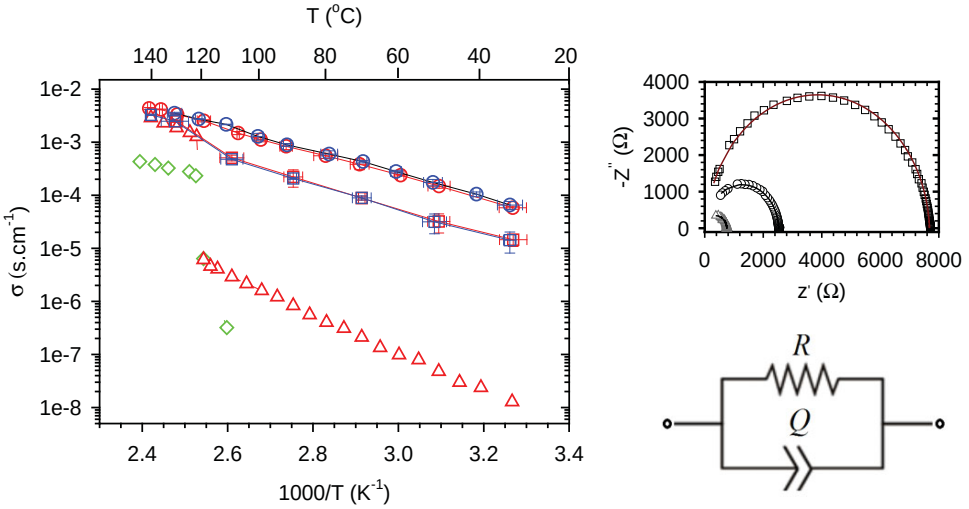

Figure 3. Left frame: Arrhenius plots of the ionic conductivities of SiO_2-$LiBH_4$ nanocomposites and bulk $LiBH_4$. The nanocomposites contain the same amount of $LiBH_4$ (42 wt%) but the degrees of pores filling are different. Circles: sample melt-infiltrated MI-91, squares: sample melt-infiltrated MI-60, green diamonds: physical-mixture PM-91, red triangles: bulk $LiBH_4$. Red symbols: measurements performed during heating runs and blue symbols during cooling runs. The jump at around 110 °C is due to the phase transition.[23] The SiO_2-$LiBH_4$ data points are an average over seven (circles) or two (squares) cycles in temperature. Top right frame: Nyquist plot obtained for the AC-EIS measurements on MI-91 at different temperatures (squares: 30 °C, circles: 50 °C, triangles: 80 °C. The dots are the experimental points, the lines the fits with (RQ) equivalent circuits (bottom right frame). R is a resistor, Q a constant phase element.

striking observation is that the low-temperature ionic conductivities for the nanocomposites are very high. For instance at 40 °C, the conductivity of MI-91 is 0.1 mS cm^{-1}, a value about three orders of magnitude higher than for the bulk $LiBH_4$ at this temperature. This is even more surprising when realizing that a large fraction of these nanocomposites consists of highly isolating SiO_2. At high temperatures, above 120 °C, the conductivities of the nanocomposites are comparable to the high temperature polymorph of bulk $LiBH_4$ with a value of 2.5 mS cm^{-1} (bulk) at 140 °C against 4 mS cm^{-1} (MI-91). The ionic conductivity is very stable in time and against temperature changes. Each data point in Figure 3, left frame, is an average over two or seven temperature cycles, from 30 to 140 °C, and the whole series of measurements were collected in two weeks, during which time no degradation was observed.

The slopes of the Arrhenius plots are different for the bulk borohydride and for the nanocomposite. For $LiBH_4$ confined in the pores of the silica scaffold, the average apparent activation energy, over the whole temperature range, is 0.43 eV for MI-91 and below 120 °C, 0.49 eV for MI-60. These values are lower than the 0.55–0.56 eV[23,56] reported for Li^+ diffusion in bulk $LiBH_4$ in the high temperature phase. The conductivity of the nanocomposite MI-60, with partial pore filling, is about a factor 2 lower than that of MI-91. This supports the fact that the conductivity in the nanocomposites is fully dominated by the very high intrinsic conductivity of $LiBH_4$ confined in the nanopores, as for MI-60 the amount of $LiBH_4$ in the pores is about half of that of MI-91. The fraction of the $LiBH_4$ in MI-60, being crystalline and outside the pores, contributes to the slight jump in the conductivity at temperatures above the structural phase transition. The physical mixture (PM-91) shows similar trends as bulk LiBH4 with an increase in the conductivity around the solid-solid phase transition. Below that temperature, the measurements are difficult as the limit of the measuring range of the potentiostat is reached. The conductivity of PM-91 is lower in magnitude than the one of bulk $LiBH_4$ as the pellet contains only 42 wt% of borohydride. It can be concluded that the scaffold has no impact on the conductivity when only physically mixed with the borohydrides.

In addition to the EIS, cyclic voltammetry measurements, performed on asymmetric pellets with only one electrode consisting of Li metal, proved the actual transport of lithium through the solid electrolyte and the absence of detectable electronic conductivity. In **Figure 4**, an example of cyclic voltammetry measurements performed on MI-91 are shown. The potential was increased from –3.5 V to 3.5 V at a rate of 20 mV S^{-1}. The current evolves linearly with the potential reflecting lithium plating (negative potentials) and stripping (positive potentials) on the electrodes. When all the plated lithium is removed from the electrode, the current falls to zero. Except the current due to the transport of Li^+ through the electrolyte, no additional current is observed, indicating the absence of any electrochemical reaction and electroactive species and hence the high stability of this solid electrolyte in this potential window. (See Supporting Information for further details).

2.3.2. Nuclear Magnetic Resonance

To study the origin of the unusually high ionic mobility in the nanocomposites, we employed solid-state nuclear magnetic

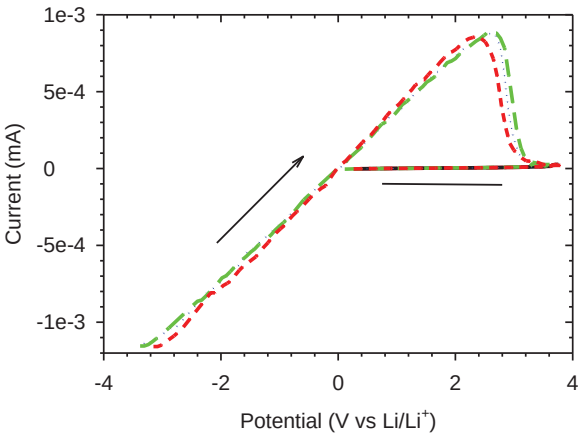

Figure 4. Cyclic voltammetry measurements performed at 40 °C on an asymmetric pellet made of MI-91, with only one electrode consisting of Li metal. The potential is increased from –3.5 V to 3.5 V and then decreased to 0 V at a rate of 20 mV S^{-1}. Green long dashed line: first measurement, blue dotted line: second measurement, red short dashed line: tenth measurement.

resonance. The dynamics in bulk $LiBH_4$ have been studied extensively by NMR. In the orthorhombic low-temperature polymorph, the NMR relaxation and line-shape parameters are mostly influenced by two different rotational jump processes of the BH_4 units.[24,57] At 110 °C, the phase transition to the hexagonal high-temperature phase is observed, which in addition to the dynamics of the BH_4 units brings about a high mobility of the Li^+ ions. This is witnessed through relaxation studies and the disappearance of dipolar broadening of the ^7Li resonance. As shown by the ^7Li MAS NMR study by Arnbjerg et al.,[33] the quadrupolar interaction of the ^7Li resonance increases upon going from the orthorhombic to the hexagonal phase, indicating a lower symmetry of the Li-site in the latter phase, despite its higher Li^+ mobility. Our ^7Li-spectra for bulk $LiBH_4$ above the transition temperature (**Figure 5**, left frame) also clearly displays the effect of a finite quadrupolar interaction (C_Q = 36.8 kHz). Rapid hopping of the Li-ions over the lattice sites results in a time averaged electric field gradient reflecting the symmetry of the crystal. As the high temperature phase is hexagonal, fast isotropic motion of the Li-ions will not average the quadrupolar interaction to zero. Based on ^6Li and ^7Li relaxometry data, Epp and Wilkening[24] report that Li^+ diffusion in the high-temperature phase of bulk $LiBH_4$ is anisotropic. Anisotropic motions will in general lead to only partial averaging of NMR interactions.

Figure 5 (middle frame) shows solid state ^7Li NMR measurements of $LiBH_4$ confined in the 4.0 nm pores of ordered mesoporous silica (MI-91) together with the evolution with temperature of the line widths of the two observed components and their relative fractions. As a reference (left frame), the spectra for bulk $LiBH_4$ are also shown. The peak widths in these spectra are a reflection of the Li^+ mobilities in the samples, with the narrower peak indicating higher mobilities averaging dipolar and quadrupolar interactions. Striking differences are observed comparing the nanocomposites to bulk $LiBH_4$. The spectrum for bulk $LiBH_4$ clearly shows a sudden transition from a phase with a low Li^+ mobility (broad peaks)

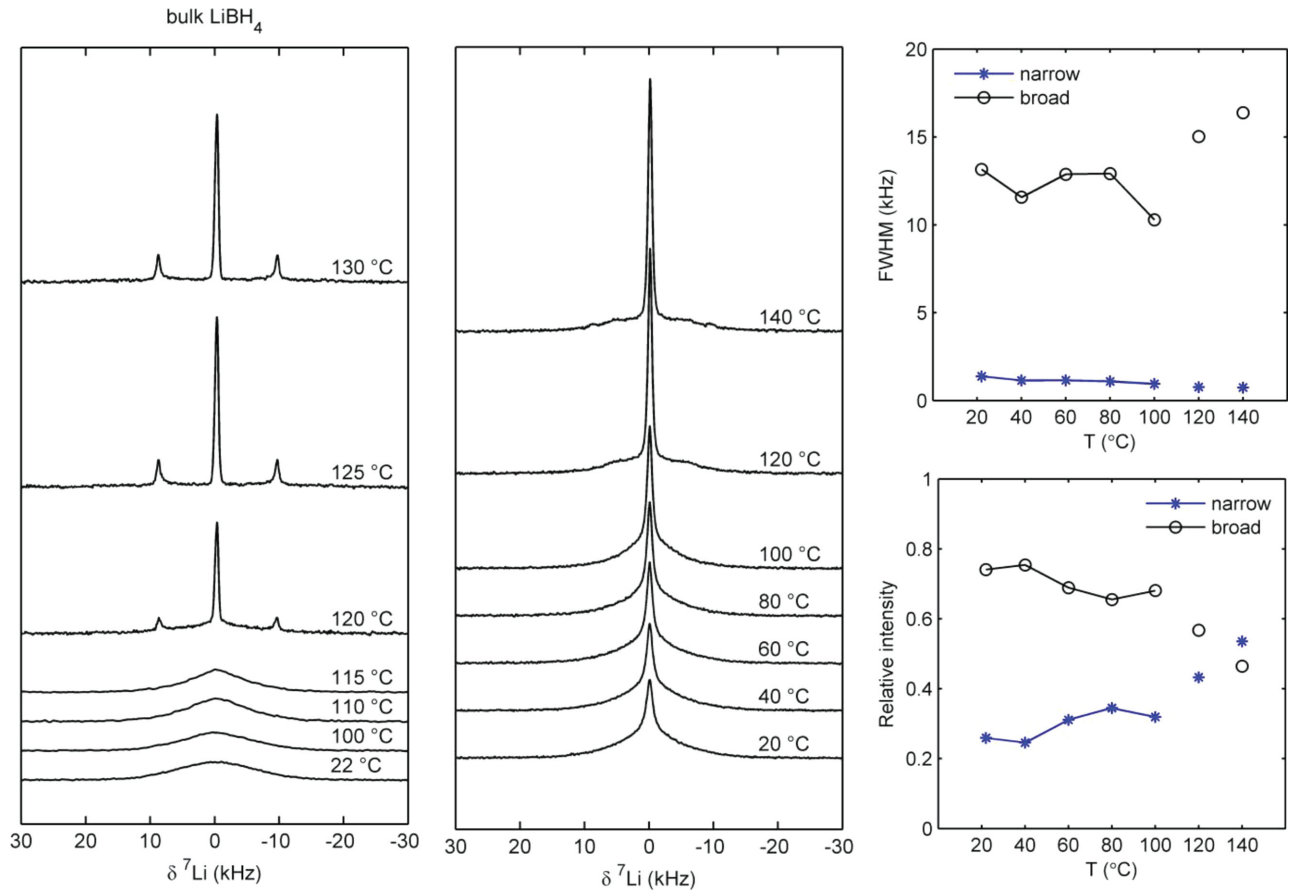

Figure 5. Static-solid state ^{7}Li NMR (with ^{1}H decoupling) measurements. Left frame: results for bulk $LiBH_4$ with the sharp phase transition from the low Li^+ mobility phase (broad lines) to the high Li^+ mobility phase (narrow lines) at temperatures close to 110 °C clearly visible. Middle frame: Results for $LiBH_4$ confined in 4.0 nm pores (MS-91 high filling degree). Remarkable is the contribution of a narrow line (high Li^+ mobility) already observed at room temperature, the absence of a clear mobility transition as a function of temperature, and the fact that lineshape deconvolution clearly indicates the presence of a more and a less mobile Li^+ fraction. Top right frame: Evolutions of the broadening of the narrow and broad lines with temperature for $LiBH_4$ confined in 4.0 nm pores (MS-91, high filling degree). Bottom right frame: Evolutions of the spectral areas of the narrow and broad lines with temperature for $LiBH_4$ confined in 4.0 nm pores (MS-91, high filling degree).

at low temperatures, to a phase with a high Li^+ mobility (narrow peaks for the central and satellite transitions of the ^{7}Li (I = 3/2) system) at high temperatures. For the nanocomposite, the peaks comprise two components; a broad line with a line width similar to that of the low-temperature bulk phase and a substantially narrower line. We interpret this as the presence of two components with different Li mobility; the broad line represents a lower Li-mobility phase and the narrow line a phase with high Li mobility. It should be noted that the broad line could also contain contributions from the satellite transitions. The narrow line is present at room temperature, indicating the existence of highly mobile Li^+ already at this temperature, in line with the high ionic conductivity found in the conductivity measurements. Assuming that the quadrupolar interaction of the narrow component is negligible, at temperatures from 20 to 100 °C a rough estimation of the spectral areas of the two components shows that about 30% comes from the highly mobile Li^+ and about 70% from Li^+ with low mobility. This means that approximately 30% of the nanoconfined $LiBH_4$ shows a high mobility at room temperature. While temperature increases, we observe a continuous narrowing of the narrow Li-resonance indicating a continuous increase of the Li^+ diffusion in line with the conductivity measurements. Unfortunately detailed analysis of the broad spectral component as a function of temperature is hampered by its complicated shape at high temperatures, which is markedly different from that of pure crystalline $LiBH_4$ above the transition temperature. It will be the topic of further studies.

The NMR results clearly show that the high ionic conductivity found for the nanocomposites at room temperature is due to the high mobility of Li^+ ions in a fraction of the nanoconfined $LiBH_4$. There is evidence of two types of Li^+, with clearly different mobilities. The very high mobility of a fraction of the Li^+ explains the high ionic conductivity measured over the whole temperature range, while the mobility of the other fraction is so much lower that it should not contribute significantly to the AC ionic conductivity measured at room temperature.

2.3.3. Nature of the Nanoconfined $LiBH_4$ and High Ionic Conductivity

It is clear from the NMR measurements that two distinct Li^+ mobilities are found for $LiBH_4$ confined in the nanopores of the SiO_2. In theory, the existence of two different types of Li^+ in a single $LiBH_4$ phase is possible, for example, by the formation of a Frenkel pair and presence of interstitial lithium.[56] However, it is more likely that the nanopores contain two different fractions of $LiBH_4$. Indications of the existence of these two fractions come from previously reported data on the mobilities in $LiBH_4$ confined in nanoporous carbon. Shane et al.[44] found, from an NMR study on $LiBH_4$ confined in 13 and 25 nm pore-size carbon aerogels, two clearly different contributions in terms of hydrogen and lithium mobility. Based on the fact that the mobile hydrogen fraction was larger in the sample with the smallest pores, they proposed a core-shell model with bulk-like core regions having slow-moving BH_4^- anions, and layers with fast-moving anions near the scaffold wall and grain boundaries. Also quasi-elastic neutron scattering (QENS) yielded data on the hydrogen mobility for carbon-confined $LiBH_4$ samples, showing fast BH_4^- rotation below the bulk structural phase transition temperature.[45,58,59] Verdal et al.[45] distinguished two quasielastic components, a narrower component presumably associated with more slowly reorienting BH_4^- anions and a broader component with much more rapidly reorienting BH_4^-. Attributing the $LiBH_4$ with the rapid reorienting BH_4^- units to an interfacial $LiBH_4$ layer near the carbon pore walls, they proposed an interfacial layer thickness of about 0.4 nm, value similar to the one obtained at room temperature by Shane et al.[44] However, it should be noted that these calculations are based on a pore size determination using Barrett-Joyner-Halenda analysis, which is known to significantly underestimate the pore sizes in the nanometer range.[60] Furthermore, the heterogeneity of the carbon scaffold pore geometry hampers such a quantitative interpretation.

In the present paper, and for the first time, data are presented on the Li^+ mobility for $LiBH_4$ confined in the monodisperse and cylindrical pores of SiO_2 scaffolds. In this case, two different mobilities are observed, with the high one existing at temperatures far below the bulk crystalline $LiBH_4$ phase transition temperature, but also below the temperature at which a fraction of the confined $LiBH_4$ undergoes a phase transition. This allows us to identify that indeed two different fractions of $LiBH_4$ are present in the pores, and that only a part of the nanoconfined $LiBH_4$ undergoes a solid-solid phase transition similar to bulk $LiBH_4$, albeit at much lower temperatures. The high Li^+ mobility measured with NMR, and also the high ionic conductivity that is reported for the first time here, are entirely dominated by $LiBH_4$ that does not undergo any measurable mobility transition. The indication for the existence of different fraction within the pores is also reinforced by the DSC measurements and the amounts of heat recorded during the phase transition of the confined borohydride and which are significantly lower than expected if all the nanoconfined $LiBH_4$ would undergo the phase transition.

In the present case, the highly defined nature of the porosity of the scaffold as well as the accurate pore size determination facilitated by the well-defined cylindrical pore geometry and smooth pore walls, allows us to quantify, accordingly to the core-shell model used by Verdal or Shane, the thickness of the conductive interfacial layer accurately. From the NMR measurements, we observed that for MI-91, 30% of the nanoconfined $LiBH_4$ exhibits high lithium mobility at room temperature. In the 4.0 nm nanopores of the MCM this means, assuming the same density for the two fractions, a shell layer thickness of 1.0 nm. However, the present measurements do not fully prove the proposed model, because the exact nature of the conductivity is not directly probed. At present, it cannot be excluded that the conductivity is only interface related and/or due to physical confinement. For instance strain could be induced by the different thermal expansion coefficients of the scaffold and the $LiBH_4$, increasing the interionic distances.[58] Further, more detailed, investigations will be necessary to unequivocally identify the origin of the observed high ionic mobility.

3. Conclusions

We present a study of the impact of $LiBH_4$ infiltration into the nanopores of ordered mesoporous SiO_2 scaffolds on its structural phase transition, Li^+ ionic mobility and ionic conductivity. Clearly two different fractions of $LiBH_4$ are present in the pores. One fraction, probably present in the center of the pores, resembles crystalline bulk $LiBH_4$ in the sense that it undergoes a solid-solid phase transition, which is shifted to lower temperatures (from 110 °C to 90 °C in the case of a 4.0 nm pore scaffold) as a result of the reduced dimensions, while NMR measurements also suggest that its structure might be slightly different from that of bulk $LiBH_4$. Surprisingly, a very high ionic conductivity for nanoconfined $LiBH_4$ is found far below the transition temperatures, with even at room temperature reaching 0.1 mS cm^{-1}, a value about three orders of magnitude larger than that of bulk crystalline $LiBH_4$ at this temperature. The very high ionic conductivity is correlated to a fast Li^+ mobility as evidenced by Li NMR measurements, which confirms that it persists to such low temperatures. At high temperatures, the conductivity of the mobile nanoconfined fraction of $LiBH_4$ is even clearly higher than that of the high temperature, high mobility phase of crystalline $LiBH_4$, especially taken into account that the nanocomposite samples also comprised 42 vol% of isolating SiO_2. No mobility transition temperature is observed for the nanoconfined $LiBH_4$, which signifies that the ionic conductivity and Li^+ mobility are dominated by the fraction of the nanoconfined $LiBH_4$ that does not undergo a solid-solid phase transition, i.e., a fraction which is probably present near the interface between the $LiBH_4$ and the SiO_2 pore walls. Due to the well-defined porosity of the scaffolds, the average thickness of this interfacial high Li^+ mobility layer is trustfully determined to be 1.0 nm for 4.0 nm pore scaffolds at room temperature.

The DSC runs, IES measurements and cyclic voltammetry curves prove that the nanocomposites are stable in temperature, up to at least 140 °C and electrochemically stable at potentials suitable for Li-ion batteries.

A better understanding of the nature of the high-mobility phase and the influence of structural parameters are expected to allow a further increase in effective ionic conductivity. Our results

point to a new strategy to design low-temperature ion conducting solids for application in all solid-state lithium ion batteries.

4. Experimental Section

Preparation of the Pore-confined $LiBH_4$: MCM-41 mesoporous scaffolds are synthesized according to the procedure reported by Cheng et al.[44] The composition of the reaction mixture is 1 SiO_2:0.25 CTAB:0.20 TMAOH:40 H_2O. Aerosil 380 is used as a silica source. The mixture is stirred at 40 °C for 1 h, and then left to age for 20 h. It is subsequently transferred to a Teflon-line steel autoclave, and hydrothermally treated for 48 h at 140–150 °C. The product is filtered, washed extensively and dried at 60 °C for 12 h and at 120 °C for 9 h and then calcined at 550 °C for 8 h. The SiO_2 scaffolds are dried again, prior to infiltration, under an Ar flow at 200 °C for at least 24 h. For the $LiBH_4$ infiltration, the required amounts of dried silica scaffold and $LiBH_4$ are mixed in a graphite sample holder and placed into a stainless steel autoclave. An initial pressure of 100 bar of H_2 is applied and the mixture is heated at 3 °C min^{-1} to 295 °C ($LiBH_4$ melting point 278 °C) and then kept at 295 °C for 25 min. at a final pressure of 180 bar of H_2. Afterwards, the impregnated scaffold is cooled down to room temperature and the hydrogen pressure released. A loading of 34 wt.% $LiBH_4$, nominally corresponds to exact filling of the total pore volume of the porous SiO_2 matrices. Typically a 20–30% higher weight loading was applied to ensure complete pore filling. All sample handling and storage is under Ar atmosphere in a glove-box (contamination typically less than 0.1 ppm of O_2 and H_2O) to avoid exposure and contamination.

Structural Characterization: Structural characterization is performed using N_2 physisorption, transmission electron microscopy (TEM) and X-ray diffraction (XRD) measurements in airtight sample holders. N_2 physisorption measurements are performed at –196 °C, using a Micromeritics Tristar 3000 apparatus. Prior to analysis, the samples are dried under N_2 for 16 h at 250 °C. Their pore size distributions are calculated from the N_2 desorption branch using the method of Barrett-Joyner-Halenda (BJH) with the Harkins and Jura thickness equation or more accurately using Non-linear Density Functional Theory calculations. TEM images are acquired with an FEI Tecnai 20F (equipped with a Field Emission Gun) and operated at 200 kV. A small amount of sample is placed on a 200 mesh Cu grid coated with a carbon polymer film in the glovebox and transferred into the microscope. The samples are exposed to air for no longer than 5 s. Energy-dispersive X-ray spectroscopy (EDX) and electron energy loss spectroscopy (EELS) are used for elemental analysis. XRD patterns are obtained at room temperature, varying 2θ from 18 to 75°, with a Bruker-AXS D-8 Advance X-ray diffractometer setup using Co$K\alpha_{1,2}$ radiation with $\lambda = 1.79026$ Å.

Calorimetry: Differential Scanning Calorimetry (DSC) measurements were performed with an apparatus from Mettler Toledo (HP DSC1). The samples were measured while ramping at 5 K/min under a pressure of 20 bar H_2 with a flow of 20 mL/min. The equipment was calibrated for temperature and heat flow under 1 bar H_2 using standard Zn, In and Al calibration references, and by using the pure $LiBH_4$ as a reference for the absolute enthalpies under hydrogen pressure (see the Supporting Information of more details).

Solid State Nuclear Magnetic Resonance (NMR): Solid-state NMR experiments were performed on a 600 MHz Varian VNMRS spectrometer using a 2.5 mm HX MAS probe. Static NMR experiments were performed in a dry N_2 gas flow because of the sensitivity of the samples to H_2O. Single Pulse Excitation (SPE) spectra of ^7Li were obtained using a 0.2 μs pulse at a rf-field strength of 140 kHz. A recycle delay of 5 s was used and no proton decoupling was applied.

Electrochemical Impedance Spectroscopy (EIS): The conductivity of the impregnated scaffolds and $LiBH_4$ is measured by alternating current impedance spectroscopy using a PARSTAT 2273 potentiostat. The bulk or nano-confined $LiBH_4$ are pressed into pellets of diameter 13 mm and thickness of 5 mm in between two lithium foils (Sigma Aldrich Co., purity 99.9%) serving as electrodes. A pressure of 1 ton/cm^2 is used, giving a final porosity estimated to be around 0.3 to 0.4. All preparation and measurements are carried under Ar atmosphere. The frequency range of the AC impedance measurements is set from 100 mHz to 1 MHz. The pellets are cycled in temperature from 30 °C to 140 °C. Before each measurement, a 60 min dwell time is used for the pellet temperature to equilibrate.

Supporting Information

Supporting Information is available from the Wiley Online Library or from the author.

Acknowledgements

The authors would like to thank Hans Meeldijk for the transmission electron microscopy, and Rien van Zwienen for support with high pressure calorimetric equipment. The authors acknowledge support from the Danish Agency for Science, Technology and Innovation (DASTI) through the project InterBat (Interfaces and Reactions in Batteries) and from the COST action MP1103. Also financial support by a grant from the Dutch organization for scientific research (NWO ACTS Sustainable Hydrogen) is gratefully acknowledged. The work results from collaboration between members of the IEA HIA Task 32.

Received: July 29, 2014
Revised: September 19, 2014
Published online: October 22, 2014

[1] M. Armand, J.-M. Tarascon, *Nature* **2008**, *451*, 652.
[2] A. Patil, V. Patil, D. W. Shin, J.-W. Choi, D.-S. Paik, S.-J. Yoon, *Mater. Res. Bull.* **2008**, *43*, 1913.
[3] P. Knauth, *Solid State Ionics* **2009**, *180*, 911.
[4] J. B. Goodenough, Y. Kim, *Chem. Mater.* **2010**, *22*, 587.
[5] Y. Kato, K. Kawamoto, R. Kanno, M. Hirayama, *Electrochemistry* **2012**, *80*, 749.
[6] J.-M. Tarascon, *Philos. Trans. A. Math. Phys. Eng. Sci.* **2010**, *368*, 3227.
[7] R. J. Brodd, W. Huang, J. R. Akridge, A. Takahara, K. Nakamura, K. Tanaka, T. Kajiyama, *Macromol. Symp.* **2000**, *159*, 229.
[8] M. Park, X. Zhang, M. Chung, G. B. Less, A. M. Sastry, *J. Power Sources* **2010**, *195*, 7904.
[9] P. Arora, Z. J. Zhang, *Chem. Rev.* **2004**, *104*, 4419.
[10] J. Y. Song, Y. Y. Wang, C. C. Wan, *J. Electrochem. Soc.* **2000**, *147*, 3219.
[11] A. G. Belous, G. N. Novitskaya, S. V. Polyanetskaya, Y. I. Gornikov, *Inorg. Mater.* **1987**, *23*, 470.
[12] Y. Inaguma, C. Liquan, M. Itoh, *Solid State Commun.* **1993**, *86*, 689.
[13] O. Bohnke, *Solid State Ionics* **2008**, *179*, 9.
[14] V. Thangadurai, J. Schwenzel, W. Weppner, *Ionics* **2005**, *11*, 11.
[15] H. Aono, E. Sugimoto, Y. Sadaoka, G.-Y. Adachi, N. Imanaka, *Solid State Ionics* **1991**, *47*, 257.
[16] K. Arbi, J. M. Rojo, J. Sanz, *J. Eur. Ceram. Soc.* **2007**, *27*, 4215.
[17] P. Bruce, A. West, *J. Electrochem. Soc.* **1983**, *130*, 662.
[18] a. Züttel, S. Rentsch, P. Fischer, P. Wenger, P. Sudan, P. Mauron, C. Emmenegger, *J. Alloys Compd.* **2003**, *356–357*, 515.
[19] Z. Łodziana, T. Vegge, *Phys. Rev. Lett.* **2006**, *97*, 119602.
[20] J. K. Kang, S. Y. Kim, Y. S. Han, R. P. Muller, W. a. Goddard, *Appl. Phys. Lett.* **2005**, *87*, 111904.
[21] D. Blanchard, Q. Shi, C. B. Boothroyd, T. Vegge, *J. Phys. Chem. C* **2009**, *113*, 14059.
[22] P. Ngene, M. R. van Zwienen, P. E. de Jongh, *Chem. Commun.* **2010**, *46*, 8201.
[23] M. Matsuo, Y. Nakamori, S. Orimo, H. Maekawa, H. Takamura, *Appl. Phys. Lett.* **2007**, *91*, 224103.

[24] V. Epp, M. Wilkening, *Phys. Rev. B* **2010**, *82*, 020301.
[25] T. Ikeshoji, E. Tsuchida, T. Morishita, K. Ikeda, M. Matsuo, Y. Kawazoe, S. Orimo, *Phys. Rev. B* **2011**, *83*, 144301.
[26] A. Unemoto, M. Matsuo, S. Orimo, *Adv. Funct. Mater.* **2014**, *24*, 2267.
[27] M. Matsuo, S. Orimo, *Adv. Energy Mater.* **2011**, *1*, 161.
[28] P. C. Aeberhard, K. Refson, W. I. F. David, *Phys. Chem. Chem. Phys.* **2013**, *15*, 8081.
[29] H. Maekawa, M. Matsuo, H. Takamura, M. Ando, Y. Noda, T. Karahashi, S. Orimo, *J. Am. Chem. Soc.* **2009**, *131*, 894.
[30] H. Oguchi, M. Matsuo, J. S. Hummelshøj, T. Vegge, J. K. Nørskov, T. Sato, Y. Miura, H. Takamura, H. Maekawa, S. Orimo, *Appl. Phys. Lett.* **2009**, *94*, 141912.
[31] R. Miyazaki, T. Karahashi, N. Kumatani, Y. Noda, M. Ando, H. Takamura, M. Matsuo, S. Orimo, H. Maekawa, *Solid State Ionics* **2011**, *192*, 143.
[32] L. H. Rude, E. Groppo, L. M. Arnbjerg, D. B. Ravnsbæk, R. a. Malmkjær, Y. Filinchuk, M. Baricco, F. Besenbacher, T. R. Jensen, *J. Alloys Compd.* **2011**, *509*, 8299.
[33] L. M. Arnbjerg, D. B. Ravnsbæk, Y. Filinchuk, R. T. Vang, Y. Cerenius, F. Besenbacher, J.-E. Jørgensen, H. J. Jakobsen, T. R. Jensen, *Chem. Mater.* **2009**, *21*, 5772.
[34] D. Sveinbjornsson, a. S. Christiansen, R. Viskinde, P. Norby, T. Vegge, *J. Electrochem. Soc.* **2014**, *161*, A1432.
[35] S. H. Tolbert, A. P. Alivisatos, *Science* **1994**, *265*, 373.
[36] C. E. Giusca, V. Stolojan, J. Sloan, F. Börrnert, H. Shiozawa, K. Sader, M. H. Rümmeli, B. Büchner, S. R. P. Silva, *Nano Lett.* **2013**, *13*, 4020.
[37] P. Buffat, J. Borel, *Phys. Rev. A* **1976**, *13*.
[38] E. Roduner, *Chem. Soc. Rev.* **2006**, *35*, 583.
[39] M. Alcoutlabi, G. B. McKenna, *J. Phys. Condens. Matter* **2005**, *17*, R461.
[40] A. F. Gross, J. J. Vajo, S. L. Van Atta, G. L. Olson, *J. Phys. Chem. C* **2008**, *112*, 5651.
[41] P. Ngene, M. H. W. Verkuijlen, Q. Zheng, J. Kragten, P. J. M. van Bentum, J. H. Bitter, P. E. de Jongh, *Faraday Discuss.* **2011**, *151*, 47.
[42] T. Sun, J. Liu, Y. Jia, H. Wang, D. Sun, M. Zhu, X. Yao, *Int. J. Hydrogen Energy* **2012**, *37*, 18920.
[43] X. Liu, D. Peaslee, C. Z. Jost, T. F. Baumann, E. H. Majzoub, *Chem.* **2011**, *23*, 1331.
[44] D. T. Shane, R. L. Corey, C. Mcintosh, L. H. Rayhel, R. C. Bowman, J. J. Vajo, A. F. Gross, M. S. Conradi, *J. Phys. Chem. C* **2010**, *114*, 4008.
[45] N. Verdal, T. J. Udovic, J. J. Rush, X. Liu, E. H. Majzoub, J. J. Vajo, A. F. Gross, *J. Phys. Chem. C* **2013**, *117*, 17963.
[46] M. H. W. Verkuijlen, P. Ngene, D. W. De Kort, C. Barre, A. Nale, E. R. H. Van Eck, P. J. M. Van Bentum, P. E. De Jongh, A. P. M. Kentgens, *J. Phys. Chem.* **2012**, *116*, 22169.
[47] R. L. Corey, D. T. Shane, R. C. Bowman, M. S. Conradi, *J. Phys. Chem. C* **2008**, *112*, 18706.
[48] A. Taguchi, F. Schüth, *Microporous Mesoporous Mater.* **2005**, *77*, 1.
[49] P. Ngene, P. Adelhelm, *J. Phys. Chem. C* **2010**, *114*, 6163.
[50] P. E. de Jongh, T. M. Eggenhuisen, *Adv. Mater.* **2013**, *25*, 6672.
[51] S. Orimo, Y. Nakamori, G. Kitahara, K. Miwa, N. Ohba, S. Towata, a. Züttel, *J. Alloys Compd.* **2005**, *404–406*, 427.
[52] Y. Nakamori, K. Miwa, A. Ninomiya, H. Li, N. Ohba, S. Towata, A. Züttel, S. Orimo, *Phys. Rev. B* **2006**, *74*, 1.
[53] N. M. Beekmans, L. Heyne, *Electrochim. Acta* **1976**, *21*, 303.
[54] S. Haile, D. West, J. Campbell, *J. Mater. Res.* **1998**, *13*, 1576.
[55] D. Sveinbjörnsson, J. S. G. Myrdal, D. Blanchard, J. J. Bentzen, T. Hirata, M. B. Mogensen, P. Norby, S. Orimo, T. Vegge, *J. Phys. Chem. C* **2013**, *117*, 3249.
[56] J. S. G. Myrdal, D. Blanchard, D. Sveinbjörsson, T. Vegge, *J. Phys. Chem. C* **2013**, *117*, 9084.
[57] K. Jimura, S. Hayashi, *J. Phys. Chem. C* **2012**, *4*.
[58] A. Remhof, P. Mauron, A. Zu, J. P. Embs, Ł. Zbigniew, P. Ngene, P. De Jongh, *J. Phys. Chem. C* **2013**, *117*, 3789.
[59] X. Liu, E. H. Majzoub, V. Stavila, R. K. Bhakta, M. D. Allendorf, D. T. Shane, M. S. Conradi, N. Verdal, T. J. Udovic, S.-J. Hwang, *J. Mater. Chem. A* **2013**, *1*, 9935.
[60] P. I. Ravikovitch, D. Wei, W. T. Chueh, G. L. Haller, A. V. Neimark, *J. Phys. Chem. B* **1997**, *101*, 3671.